Journal of Materials Chemistry B

ROYAL SOCIETY OF CHEMISTRY

PAPER

View Article Online
View Journal | View Issue

Cite this: J. Mater. Chem. B, 2025, 13, 3864

Melt electrowriting of bioglass-laden poly(ε-caprolactone) scaffolds for bone regeneration

Ana Beatriz Gomes de Carvalho, [ab] Lais Medeiros Cardoso, [ac] Caroline Anselmi, [ad] Renan Dal-Fabbro, [a] Tiago Moreira Bastos Campos, [e] Alexandre Luiz Souto Borges, [b] Guilherme de Siqueira Ferreira Anzaloni Saavedra [b] and Marco C. Bottino *[af]

Novel and promising biomaterials for bone tissue engineering have been investigated over the years. Aiming to contribute to this progress, this study developed and evaluated polycaprolactone (PCL) scaffolds with 5% (w/w) 58S-bioactive glass (58S-BG) fabricated *via* melt electrowriting (MEW). Morphological and chemical characterization of the scaffolds was conducted. The biological potential was assessed *in vitro* with alveolar bone-derived mesenchymal stem cells through cytotoxicity, adhesion, protein production, alkaline phosphatase activity, and mineral nodule formation assays. *In vivo*, scaffolds implanted in rats were analyzed for biocompatibility, inflammation, and degradation using H&E staining and immunohistochemical markers for angiogenesis and macrophage polarization. Statistical analysis was performed at a 5% significance level. Appropriate fiber alignment but a higher fiber diameter was found for PCL + BG5% compared to PCL scaffolds (p = 0.002). EDS spectra confirmed the presence of BG's chemical components for BG-laden scaffolds, attesting to BG particle incorporation into the filaments. Raman spectroscopy evidenced the chemical nature of the BG powder, and FTIR spectra revealed –OH stretching for PCL + BG5%, evidencing its hydrophilic potential. None of the scaffolds were cytotoxic, and BG-laden formulation increased cell viability after 7 days (p = 0.0006), also showing greater cell adhesion/spreading over time compared to pristine PCL scaffolds. BG's presence also increased the mineral matrix formation ($p \leq 0.0021$) over 21 days and retained ALP activity after 14 days (p = 0.705) compared to PCL. *In vivo*, PCL scaffolds retained fiber alignment and preserved their volume throughout the evaluation, showing minimal structural alteration. In contrast, PCL + BG5% scaffolds showed more visible structural changes at 28 days. Despite this, the PCL + BG5% formulation remained biocompatible and significantly promoted angiogenesis compared to pristine PCL scaffolds. In sum, BG-laden scaffolds were successfully melt electrowritten, retaining the scaffolds' porous architecture, showing appropriate properties, including cell viability, adhesion, mineralized nodule deposition, biocompatibility, and angiogenesis, indicating that these materials are a promising alternative for enhancing bone tissue regeneration.

Received 22nd December 2024,
Accepted 14th February 2025

DOI: 10.1039/d4tb02835j

rsc.li/materials-b

1. Introduction

Additive manufacturing (AM) has been widely used for bone tissue engineering by printing biomaterials and producing scaffolds using a well-controlled layer-by-layer approach that can be successfully applied for reconstructive and regenerative treatments.[1,2] When using AM techniques, a computer-aided design (CAD) is created with the desired shape and size of the scaffold, which is later 3D printed in high precision.[3] Furthermore, one of the most significant advantages of AM is combining imaging techniques (*i.e.*, cone-beam computed tomography) with the CAD design and producing

[a] Department of Cariology, Restorative Sciences, and Endodontics, School of Dentistry, University of Michigan, Ann Arbor, MI, USA. E-mail: mbottino@umich.edu
[b] Department of Dental Materials and Prosthodontics, São Paulo State University, São José dos Campos, SP, Brazil
[c] Department of Dental Materials and Prosthodontics, São Paulo State University, Araraquara, SP, Brazil
[d] Department of Morphology and Pediatric Dentistry, São Paulo State University, Araraquara, SP, Brazil
[e] Department of Prosthodontics and Periodontology, São Paulo University, Bauru, SP, Brazil
[f] Department of Biomedical Engineering, College of Engineering, University of Michigan, Ann Arbor, MI, USA

patient-specific designs that successfully match the desired area to be regenerated.[3–5]

Melt electrowriting (MEW) is one of the most promising AM techniques, in which micro- and nanoscale filaments are produced by applying high voltage to the melted polymer collected on a moving platform.[6] It results in a thinner and highly aligned continuous filament that improves the microgeometry of the scaffolds and controls the porosity level, which is highly beneficial for reproducing the microarchitecture of human structures and consequently enhancing tissue engineering for biomedical applications.[7–10] Moreover, it is also possible to determine the fibers' diameter and perform fine adjustments by controlling the printing parameters, such as printing speed, voltage, pressure, and distance from the platform.[6,11]

Poly(ε-caprolactone), also known as PCL, has been shown to be the most used polymer for producing different scaffolds for a wide range of tissue engineering applications,[4] including MEW scaffolds.[12–14] Among the properties of this polymer, its low melting point temperature, rapid solidification, and biocompatibility are significant advantages.[7,15] However, a key disadvantage of PCL is the polymer's natural hydrophobicity, which impairs the scaffold's integration with human tissues.[10,16] In this regard, some alternatives have been investigated, such as surface treatments and/or incorporation of inorganic particles (*i.e.*, bioactive glasses, bioceramics, *etc.*) to improve the hydrophilicity or surface bioactivity.[8,17–19] In terms of incorporating particles into the polymeric matrix, the main challenge is integrating inorganic materials without significantly affecting the viscosity of the polymer, which can impair the printing process.[20]

Among the inorganic particles that can be added to PCL, bioactive glasses (BGs) consist of small particles commonly incorporated into scaffolds or hydrogels. These materials can chemically bond to natural tissues in physiological environments, mediating biological responses.[21–23] One of the greater advantages of BGs is that they induce different responses according to their composition, leading to the continuous release of bioactive ions over time.[24,25] In general, this class of materials are known for promoting cell differentiation and their osteogenic and angiogenic potential.[26,27] Over the years, various BG formulations have been developed, with chlorine-based 58S BG emerging as a promising candidate for bone regeneration due to its particle homogeneity and strong interaction with natural tissues.[28] Furthermore, when incorporated into PCL scaffolds, 58S BG demonstrated favorable biological activity.[29]

Considering the limitations of PCL and the great potential of bioglasses, this study aims to produce, characterize, and analyze (*in vitro* and *in vivo*) MEW PCL scaffolds incorporated with 58S BG as a novel approach for enhancing bone regeneration. We hypothesize that BG-laden scaffolds will be successfully printed, retaining the desired porous architecture and representing promising biomaterials for improving bone regeneration by enhancing cell viability/attachment and mineral production and retaining biocompatibility over time.

2. Materials and methods

2.1 58S Bioglass fabrication

58S bioglass (BG) was fabricated through the sol–gel method.[29] Briefly, sodium metasilicate was dissolved in an aqueous solution (10% w/w) containing an ion exchange resin to form silica sol through the exchange of Na^+ and H^+ ions, producing silicic acid (H_4SiO_4) to be used as a silica precursor. After this process, this solution was filtered with a vacuum pump. The final concentration was 60% H_4SiO_4, 36% $CaCl_2$, and 4% $NH_4H_2PO_4$, which was determined by titrating the silicic acid with standardized sodium hydroxide from which it was previously obtained. Then, the solution was dried inside an oven at 100 °C for 12 hours, followed by the calcination process for 5 hours at 500 °C. After calcination, the bioglass was crushed and sieved using a 325 mesh (45 μm).

2.2 Printing scaffolds by melt electrowriting

The scaffolds with 8 × 8 mm dimensions, 500 μm spacing, and 200 layers were designed using BioCAD software and fabricated using a multi-head 3D printer (3D Discovery, RegenHU Ltd, Villaz-St-Pierre, Switzerland) (Fig. 1(A)). For pure PCL scaffolds, the material (PCL, M_n: 5000, Cellink, Gothenburg, Sweden) was loaded into a metal cartridge and heated at 90 °C for 30 minutes to obtain a homogeneous polymer melt with appropriate flowability during printing. Then, the scaffolds were printed using a 26G needle at 0.08 MPa pressure, 40 mm s^{-1} feed rate, 7 kV voltage, and 4 mm distance from the platform. For PCL + BG5% scaffolds (w/w), BG powder was dried at 100 °C for 1 hour, then manually mixed with PCL and loaded into the metal cartridge. Then, the mixture was heated at 100 °C for 30 minutes, and the scaffolds were printed using a 24G needle at 0.150 MPa, 70 mm s^{-1} feed rate, 5.8 kV voltage, and 3 mm distance from the platform. Those printing parameters were selected based on the literature and multiple pilot studies, where the parameters were adjusted to both materials to achieve the best fiber alignment, providing an appropriate scaffold architecture and number of printed layers.

2.3 Morphological and chemical characterization

2.3.1 SEM and EDS analyses. Morphological and chemical characterization of scaffolds was performed by scanning electron microscopy (SEM) and energy dispersive spectroscopy (EDS). The scaffolds (n = 3) were gold-sputtered for 90 seconds (~10 μm) and then analyzed by using a Tescan MIRA 3 (Tescan MIRA3 FEG-SEM, Tescan USA Inc., Warrendale, PA, USA) at magnifications of 100× (with a scale bar of 500 μm), 200× (with a scale bar of 200 μm), and 1000× (with a scale bar of 50 μm). The higher magnification was used to analyze fiber diameter using the ImageJ Software (Wayne Rasband, National Institute of Health, NIH, Bethesda, MD, USA) by measuring the fibers (n = 30) in 3 different scaffolds. The mean particle size of BG powder was also analyzed using ImageJ under the same magnification. SEM was also used to evaluate the morphology of BG powder at 5000× (with a scale bar of 5 μm).

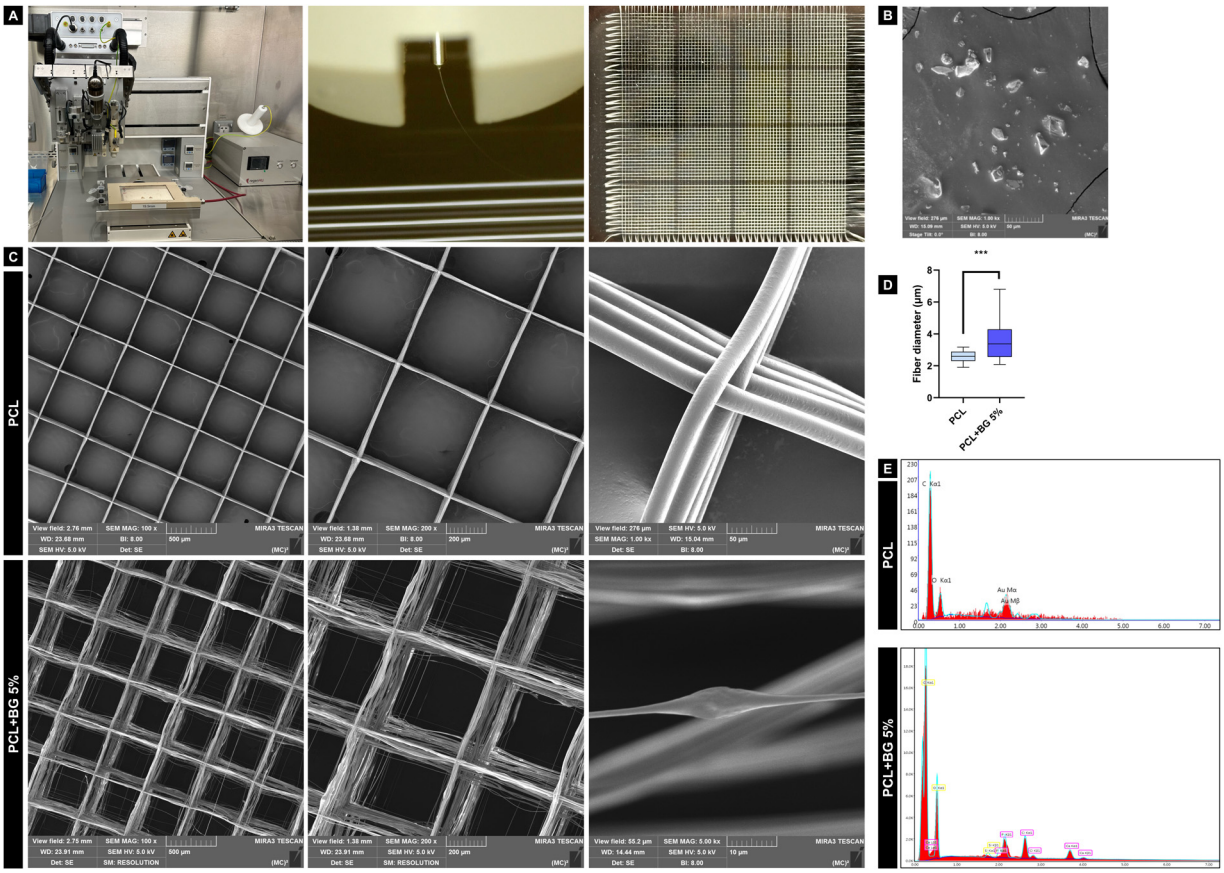

Fig. 1 (A) MEW process of PCL scaffolds; (B) SEM picture of BG particles under 10k× magnification; (C) fiber diameter of PCL and PCL + BG5% scaffolds in micrometers. Boxplots indicate median values (25th–75th percentiles). Statistical notation is indicated by *** (Mann–Whitney, $p < 0.05$); (D) SEM images of PCL and PCL + BG5% at 100×, 200×, and 5k× magnifications; and (E) EDS spectra of PCL and PCL + BG5% groups.

2.3.2 Raman spectroscopy and FTIR. The Raman spectrum of BG powder was collected using the LabRam HR Evolution spectrometer (HORIBA Scientific, Kyoto, Japan) connected to an optical microscope with a Nd:YAG laser operated at 532 nm (laser power 100%) in a spectrum range of 200–1200 cm^{-1}. Three scans were taken per sample (n = 3), considering a resolution of 600 μm and an acquisition time of 30 s. Fourier Transform Infrared Spectroscopy (ATR-FTIR, Nicolet iS50, Thermo Fisher Scientific, Inc.) was performed to analyze the chemical stretches in PCL and PCL + BG5% scaffolds. Sixteen scans were collected with a spectrum between 4000 and 500 cm^{-1} with a resolution of 4^{-1}, and the baseline correction spectra were normalized for the analysis (n = 3).

2.4 Biological assays

Alveolar bone-derived mesenchymal stem cells (aBMSCs) were previously isolated and characterized for $CD73^+$, $CD90^+$, and $CD105^+$ mesenchymal stem cell markers.[30,31] These cells were grown in a 75-cm^2 cell-culture flask (Corning, New York, NY, USA) with complete minimum essential media (α-MEM containing L-glutamine, ribonucleosides, deoxyribonucleosides, 15% fetal bovine serum/FBS and 1% penicillin–streptomycin; all from Gibco), at 37 °C and 5% CO_2. Subculture procedures were performed using 0.25% trypsin/EDTA solution (Gibco), and the cells from passages 4–7 were used for all the biological assays.

2.4.1 Cell viability. For cell viability assessment (n = 5), the scaffolds were sterilized with UV light for 1 hour on each side and placed in ultra-low attachment 24-well cell culture plates (Costar – Corning, New York, NY, USA). Additional disinfection treatment was performed by adding 1 mL of 70% ethanol to the scaffolds for 10 minutes, followed by washing with sterile PBS (Gibco) two times for 5 minutes each. Next, 1 mL of complete α-MEM was added to the scaffolds for 30 minutes. After this period, the medium was aspirated, 3×10^4 cells were seeded on the surface of the scaffolds, and samples were incubated for 1 hour to allow the initial attachment of cells to the scaffolds. Then, 1 mL of complete culture media was added to the samples, and the cells were cultured for 1, 3, and 7 days. After the pre-determined time points, the media were aspirated and replaced with 10% alamarBlue solution (Invitrogen, Carlsbad, CA, USA) in serum-free media for 3 hours at 37 °C. AlamarBlue assay is based on reducing the resazurin compound to resorufin by viable cells, resulting in a pronounced solution color change. The fluorescence intensity was assessed at 560 and 590 nm (SpectraMax iD3, Molecular Devices, LLC, San Jose, CA, USA). The mean fluorescence intensity values were converted to percentages and compared to the control group (pristine PCL

scaffolds at day 1, arbitrarily set to represent 100%) to determine the cell viability at each time point.

2.4.2 Cell adhesion and spreading. To analyze the cell adhesion and spreading of aBMSCs on the scaffolds' surface (n = 4), 3 × 10^4 cells were seeded on top of the scaffolds as previously described. Then, after 1, 3, and 7 days of culture, the cells were fixed using 4% paraformaldehyde (Sigma Aldrich, St. Louis, MO, USA), followed by washing with PBS (Gibco) and staining with a red fluorescent dye for actin filaments (1:20 in PBS; ActinRed 555 ReadyProbes reagent; Invitrogen) for 30 min and with a blue fluorescent dye DAPI (1:5000 in PBS; Thermo Fisher Scientific, Waltham, MA, USA) for nuclei, following the manufacturer's recommendations. Stained scaffolds were observed at 4× magnification using a fluorescence microscope (ECHO Revolve Microscope; Discover Echo Inc., San Diego, CA, USA).[32]

2.4.3 Alkaline phosphatase and total protein assays. To perform alkaline phosphatase (ALP) activity and total protein assays, 5 × 10^4 cells were seeded on top of the scaffolds (n = 6) and cultured for 14 days under basal and osteogenic (10 mM β-glycerolphosphate, 100 nM dexamethasone, and 50 mg mL^{-1} ascorbic acid) medium conditions. Total protein assay was performed using the Pierce™ BCA Protein Assay Kit. ALP assay was performed using the Sensolyte pNPP ALP Kit (AnaSpec Inc., Freemont, CA, USA) according to the manufacturer's recommendations. Briefly, the cells were lysed using Triton X-100, and the supernatant was collected and transferred to a 96-well plate to quantify total protein and ALP activity. After sample preparation, for the total protein assay, the supernatant was mixed with the working reagent and incubated at 37 °C for 30 minutes, and the absorbance was read at 562 nm (SpectraMax iD3). Meanwhile, the pNPP reagent was added to each well for the ALP assay, incubated for 1 hour at room temperature, and absorbance was read at 405 nm. Total protein and ALP activity concentrations were calculated using a standard curve, and ALP values were normalized according to the total protein quantification.[33]

2.4.4 Mineral nodule deposition. The mineral deposition was evaluated after 14 and 21 days of culture under basal and osteogenic (complete media supplemented with 10 mM β-glycerolphosphate, 100 nM dexamethasone, and 50 mg mL^{-1} ascorbic acid) medium conditions. aBMSCs at a density of 5 × 10^4 were seeded on top of the scaffolds and incubated according to the different time points (n = 6). After 14 and 21 days, scaffolds were fixed with 70% ethanol for 1 hour at 4 °C, washed with distilled water, and incubated with Alizarin Red staining solution (40 mM; pH 4.2) for 20 minutes under agitation (300 rpm). Then, the scaffolds were washed with distilled water 10 times until all the staining was washed out from the samples. Nodules were dissolved in 10% of hexadecylpyridinium chloride monohydrate (w/v in PBS, Sigma Aldrich, St. Louis, MO, USA) for 1 hour; next, the supernatant was collected, and the absorbance was read at 570 nm (SpectraMax iD3). PCL and PCL + BG5% scaffolds without the cells were used as background control to discount the natural staining presented by the scaffolds. The mean absorbance values were converted to percentages and compared to the control group (pristine PCL scaffolds at day 14, arbitrarily set to represent 100%).

2.5 Subcutaneous *in vivo* rat model

Six 10-week-old male Fischer 344 rats, weighing approximately 300 grams, were obtained from Envigo RMS, Inc., located in Oxford, MI, USA. The rats were divided into three groups (n = 2 rats per time point), with each rat receiving three scaffolds from each group (n = 6 scaffolds per time point) to evaluate the biocompatibility at 7, 14, and 28 days. The research protocols, including all animal handling and experimental procedures, received approval from the local Institutional Animal Care and Use Committee (IACUC) under the approval number PRO00010329, ensuring compliance with established guidelines for animal experimentation. The surgical interventions were performed under a general anesthetic regime, utilizing 50 mg kg^{-1} of ketamine (Hospira, Inc., Lake Forest, IL, USA) and 5 mg kg^{-1} of xylazine (Akorn, Inc., Lake Forest, IL, USA) delivered intraperitoneally. Six V-shaped incisions, each 2 cm long, were created with a size 15 scalpel in the prepared area of the animals' backs (Fig. 5(A)). Into these incisions, square-shaped scaffolds measuring 10 mm by 10 mm of PCL and PCL + 5%BG were randomized. Post-surgery, the wounds were stitched using Coated Vicryl® polyglactin 910 suture material (Ethicon Endo-Surgery, Inc., Cincinnati, OH, USA), allowing recovery. At predetermined intervals post-implantation, the rats were euthanized *via* CO_2 overdose.

2.6 Histological and immunohistochemical analyses

The tissues surrounding the implants and scaffolds were collected, fixed in 10% buffered formalin overnight, paraffin-embedded, and sectioned into slices 6-μm thick. These sections were subsequently stained with hematoxylin and eosin (H&E) to examine for inflammatory response and scaffold degradation. For immunostaining, the following primary antibodies were used: anti-CD31 (ab182981, Abcam, Cambridge, MA, USA) and anti-von Willebrand Factor (ab6994, Abcam) for angiogenesis, and anti-iNOS (ab283655, Abcam) and anti-CD163 (ab182422, Abcam) for macrophage polarization. All antibodies were diluted 1:100 and incubated overnight at 4 °C. Secondary staining was performed using Goat Anti-Rabbit IgG H&L (Alexa Fluor® 488, ab150077, Abcam) at 1:100 dilution for 1 hour at room temperature. Cell nuclei were counterstained with DAPI VECTASHIELD Antifade mounting media. Images were captured at 10× magnification using an ECHO Revolve microscope (BICO Company, San Diego, CA, USA). Positive immunofluorescence staining was quantified using ImageJ software by analyzing six randomly selected images per group, splitting the color channels, and measuring the fluorescence-expressed areas to calculate the percentage of positively stained regions.[34–36]

2.7 Statistical analysis

After data collection for all the mentioned tests, the Shapiro-Wilk and Levene tests assumed normality and homoscedasticity.

ANOVA and *post-hoc* tests were selected considering $\alpha = 0.05$. Fiber diameter data were the only one that did not present normal distribution (Kolmogorov–Smirnov), so a non-parametric test (Mann–Whitney) was chosen to analyze the data in particular. Microsoft Excel software (Microsoft, Redmond, Washington, USA) was used to organize the data, and GraphPad PRISM (GraphPad Software, Inc., La Jolla, CA, USA) was used for statistical analysis and graph designing.

3. Results

3.1 Morphological and chemical characterization

3.1.1 SEM and EDS analyses. The SEM picture of BG powder is presented in Fig. 1(B), which evidences the crystal shape of the particles, with an average particle size of 9.65 ± 2.86 μm. SEM pictures of PCL and PCL + BG5% printed scaffolds are presented in Fig. 1(C), which evidence that appropriate fiber alignment was achieved for both groups. Rougher filaments can be identified for the BG-laden group, evidencing the presence of the BG particle inside the polymer filament, while pure PCL scaffolds exhibit a smoother surface. SEM images were used for measuring the fiber diameter of scaffolds, and the results displayed in the graph showed an increase in fiber diameter for PCL + BG5% fibers (∅ 3.5 ± 1.7 μm) when compared to PCL scaffolds (∅ 2.58 ± 0.36 μm) ($p = 0.002$) (Fig. 1(D)). EDS spectra attested the presence of BG components such as Si, Cl, and Ca in the PCL + BG5% scaffolds, confirming the incorporation of BG into the polymer (Fig. 1(E)).

3.1.2 Raman spectroscopy and FTIR. The Q_n structure evidenced in the Raman spectra (Fig. 2(A)) is related to the structure of silicate glasses. It shows the number (n) of bridging bonds between silicon and oxygen atoms, which form a siloxane bond (Si–O–Si). This n indicates the average number of bridging bond atoms linked to silicon, varying from 0 (Q_0) to 4 (Q_4). When chemical network modifiers are added to the structure (*i.e.*, calcium, sodium, or potassium), the bridging bonds break, forming non-bridging bonds (NBOs). This means that silica glass without network modifiers predominantly exhibits a Q_4 structure, and adding modifiers leads to a decrease in the number of siloxane bonds in the system (decrease in "n"). Thus, the presence of Q_2 in the Raman graph evidences the expected structure for BG, which indicates its bioactivity potential.

The FTIR graph of BG powder, PCL, and PCL + BG5% is shown in Fig. 2(B). Regarding the BG powder, the spectra revealed a peak at ∼3600 cm^{-1} wavenumber, which corresponds to –OH stretching, another peak at ∼1000–1030 cm^{-1}, which corresponds to Si–O–Si, and a peak at ∼700–850 cm^{-1} corresponding to SiO_4. The main characteristic peaks for PCL are located at ∼1730 and ∼1295 cm^{-1} wavelengths, which correspond to C═O and C–C/C–O stretches, respectively. Finally, for PCL + BG5%, besides the characteristic peaks for PCL, it is possible to observe the OH stretch around 3600 cm^{-1}, which was present for BG powder.

3.2 Biological assays

3.2.1 Cell viability and adhesion. After 1 day of culture, the cells seeded on both PCL and PCL + BG5% scaffolds presented viability statistically similar ($p > 0.05$); however, after 3 and 7 days of culture, the cells seeded on BG-containing scaffolds showed a significantly higher viability compared to PCL scaffolds ($p < 0.05$) (Fig. 3(A)). In addition, by comparing the same group within each time-point, it was found that the cells seeded on PCL scaffolds did not present increased viability over time; on the other hand, PCL + BG5% scaffolds supported cell viability over time, which can be correlated with increased cell proliferation.

The fluorescence pictures in Fig. 3(B) provide a qualitative analysis of the cells' adhesion and spreading when in contact with the scaffolds. When comparing the scaffolds at 1, 3, and 7 days, it is possible to observe more cells attached to the pristine PCL scaffolds at the latest time points compared to the initial condition. However, this difference is even more evident when the images of the PCL + BG5% group are observed,

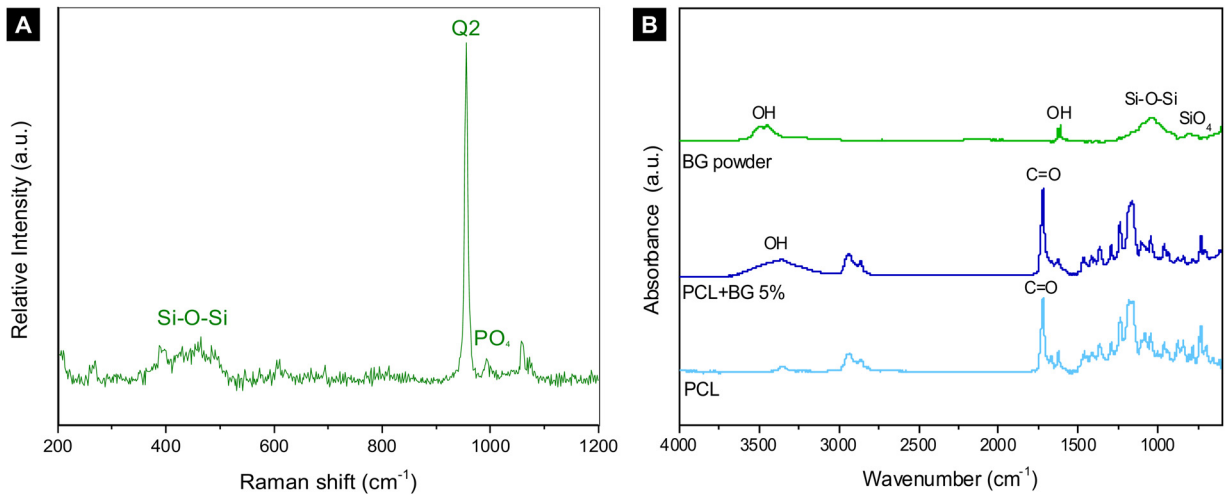

Fig. 2 (A) Raman spectrum of BG powder; (B) FTIR graph of BG powder, PCL, and PCL + BG5% indicating the chemical stretches present in each group.

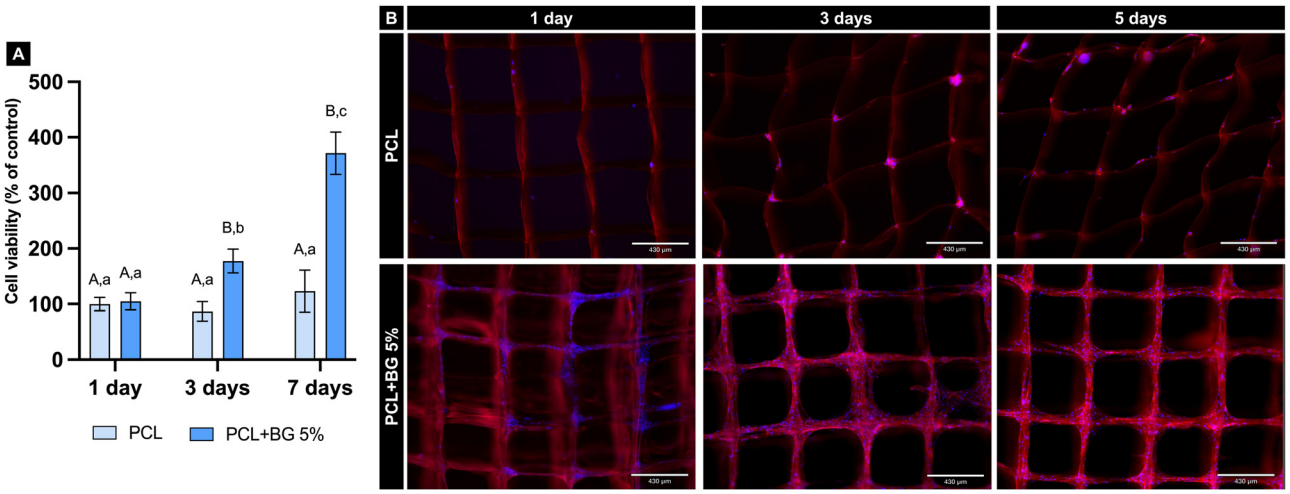

Fig. 3 (A) Cell viability assay (Alamar Blue) of alveolar bone-derived mesenchymal stem cells (aBMSCs) seeded on top of the scaffolds after 1, 3, and 7 days. Different capital letters indicate significant differences between groups within each time point, and different lowercase letters indicate significant differences between time points within each group (repeated measures ANOVA/Sidak *post-hoc*; $n = 5$; $\alpha = 0.05$). (B) aBMSC adhesion and spreading on top of scaffolds of PCL and PCL + BG5% groups after 1, 3, and 7 days ($n = 4$). Cell nuclei are stained in blue (DAPI), and actin filaments are stained in red (ActinRed). The scale bar represents 430 μm (4× magnification).

indicating considerably higher cell adhesion for the scaffolds of the BG-laden group for all the analyzed time points.

3.2.2 Osteogenic potential of scaffolds. ALP and alizarin red assays were used to analyze the osteogenic potential of PCL and PCL + BG5% scaffolds. Regarding ALP activity, it was observed that despite a lower activity demonstrated by the PCL + BG5% scaffolds under basal medium conditions, ALP activity was comparable to PCL in the presence of osteogenic media after 14 days ($p = 0.705$) (Fig. 4(A)).

Mineral nodule deposition was evaluated considering basal and osteogenic media. Considering basal media, both groups increased the mineral deposition over time, with statistically significant higher deposition for PCL + BG5% (Fig. 4(B)). On the other hand, no statistical difference was found for pristine PCL when comparing the time points in the presence of osteogenic media (Fig. 4(C)). Thus, regardless of the media condition, BG-laden scaffolds showed increased mineral nodule deposition over 21 days ($p = 0.0021$) (Fig. 4(D)).

3.3. Subcutaneous *in vivo* rat model

In vivo, PCL + BG5% demonstrated an inflammation profile similar to PCL after 7 and 14 days. After 7 days, PCL had an average of 4780 ± 302 inflammatory cells, while PCL + BG5% showed a higher average of 5433 ± 350. After 14 days, the average for PCL was 5124 ± 198. The PCL + BG5%, however, had a lower average of 5039 ± 605. By the 28-day mark, the PCL's average had decreased significantly to 2920 ± 432, while PCL + BG5% showed a decrease to 3968 ± 146 inflammatory cells (Fig. 5(B)). Throughout all evaluated time points, no statistical difference was observed in the number of inflammatory cells in contact with or surrounding the scaffold resulting from the material's implantation. This indicates the biocompatibility of the scaffold enriched with bioactive glass. Regarding the degradation and maintenance of the original architecture, PCL retained the alignment of the fibers and volume with minimal disturbance compared to PCL + BG5% throughout all the time points. Moreover, the BG-enriched scaffold presented less material remaining at 28 days (Fig. 5(C)).

Immunolabeling profiles for the evaluated markers (CD31, vWF, iNOS, and CD163) revealed significant differences over time, particularly between groups. Both CD31 and vWF, markers associated with endothelial cells and angiogenesis, exhibited consistently higher staining areas in PCL + BG5% implants compared to PCL-only implants at all examined time points (7, 14, and 28 days), indicating enhanced neovascularization in the presence of bioactive glass (Fig. 6(A)-a and (B)-b). Similarly, iNOS, an enzyme linked to a pro-inflammatory M1 macrophage phenotype, initially showed elevated levels in the PCL + BG5% group, reflecting an early but controlled inflammatory response that may facilitate tissue remodeling. Notably, this response did not persist at later intervals, suggesting a natural resolution of inflammation without compromising overall tissue integrity. In contrast, CD163, a marker of anti-inflammatory M2 macrophages, showed no statistically significant differences between groups across the study period, suggesting that BG did not markedly alter the shift toward M2-driven resolution of inflammation (Fig. 6(C)-c and (D)-d).

4. Discussion

The present study successfully produced PCL scaffolds with or without 5% 58S-BG *via* MEW as an alternative approach to induce bone regeneration. PCL was chosen for its versatile properties in tissue engineering applications, including its capacity to blend with organic and inorganic components, expanding the material's functional potential.[7,15] BG was also selected to be incorporated into the polymer because its surface

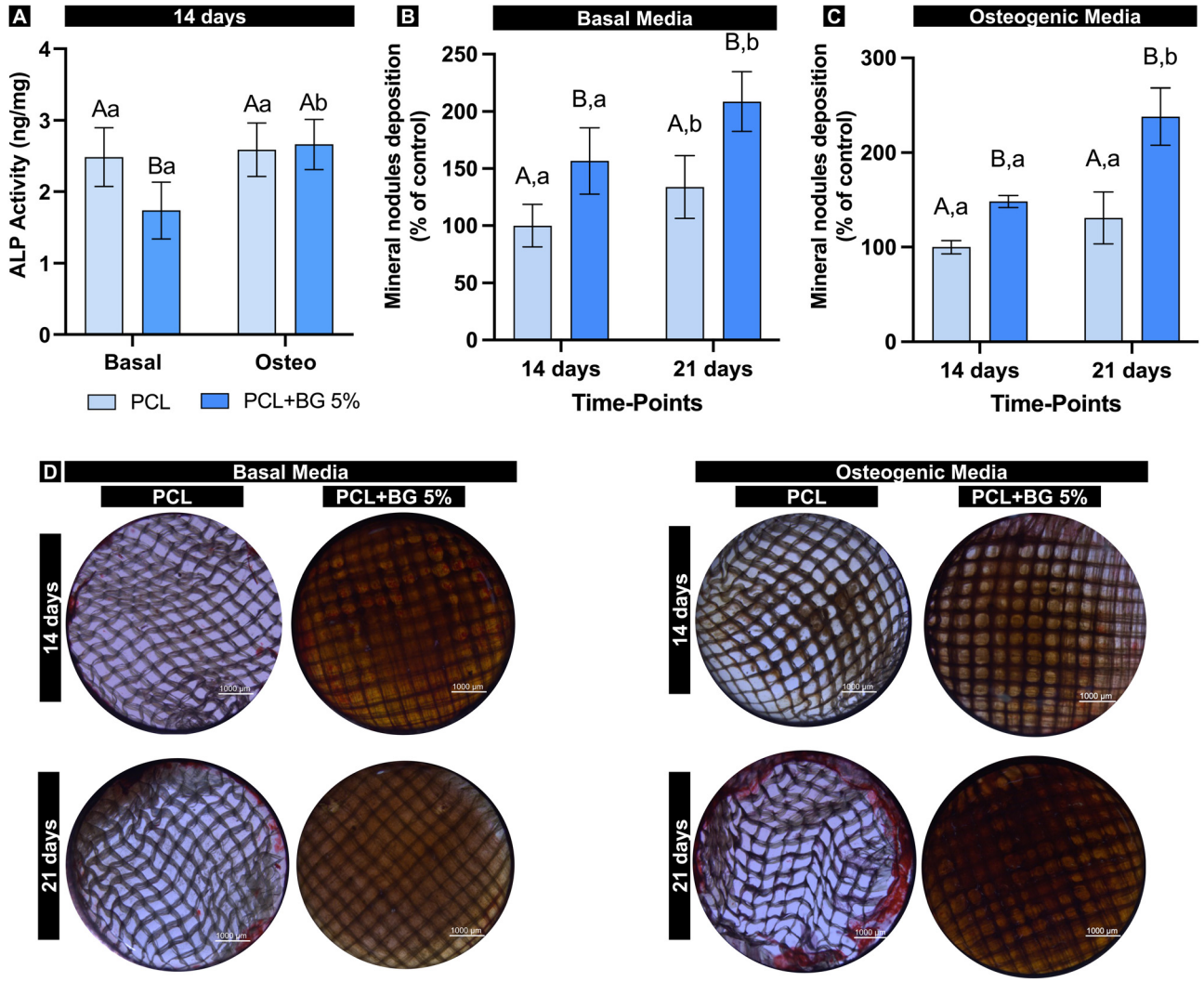

Fig. 4 (A) ALP activity (ng mg^{-1}) after 14 days of culture (n = 8) in different types of media. Different capital letters indicate statistical differences between groups under each condition. Different lowercase letters indicate statistical differences between conditions within each group; mineral nodule deposition (% of control) on the scaffolds' surface of PCL and PCL + BG5% groups after 14 and 21 days of culture, considering (B) basal and (C) osteogenic media (alizarin red assay; n = 6). Different capital letters indicate a significant difference between groups within each time point, and different lowercase letters indicate a significant difference between time points within each group (two-way ANOVA/Sidak *post-hoc*; α = 0.05); and (D) qualitative analysis of mineral nodule deposition on the scaffolds' surface after 14 and 21 days (alizarin red assay; scale bar 1000 µm).

can create a biologically active layer that binds to natural tissues while releasing ions stimulating the formation of new tissue.[21,37,38] 58S-BG has been linked to osteogenesis and angiogenesis, promoting new bone formation at scaffold and natural bone interfaces.[37] Produced using a sol–gel method, it allows fine control over textural characteristics and ion release.[39] Specifically, Si^{4+} ions strongly stimulate bone regeneration, while Ca^{2+} ions assist angiogenesis.[40,41] Moreover, the 58S chlorinated BG used here contains naturally occurring chlorine, further enhancing its biological potential.[42]

SEM analysis revealed an uneven surface of the filaments in the PCL + BG (5%) scaffolds, correlating with EDS results confirming the presence of BG components (Si, Cl, and Ca). The increased fiber diameter indicated successful BG particle incorporation into the polymer. Higher BG concentrations (>5%) were not printable due to excessive viscosity causing needle clogging, a challenge also noted in previous studies.[23] The polymer's higher viscosity results in greater resistance during the printing process, mainly when the polymer flows through the needle tip. This inconvenience leads to particle accumulation and needle clogging, interrupting printing.[20] Despite the morphological differences, the printed scaffolds exhibited appropriate filament alignment and retained the intended 500 µm spacing. Various pore sizes (100–1000 µm) have been explored in the literature,[43,44] influencing cellular behavior, and our choice of 500 µm spacing has proven effective for cell infiltration, attachment, and proliferation.[43] Additionally, the scaffolds were designed with a 0–90° grid structure, a topography arrangement that is favorable to promote bone repair.[45,46]

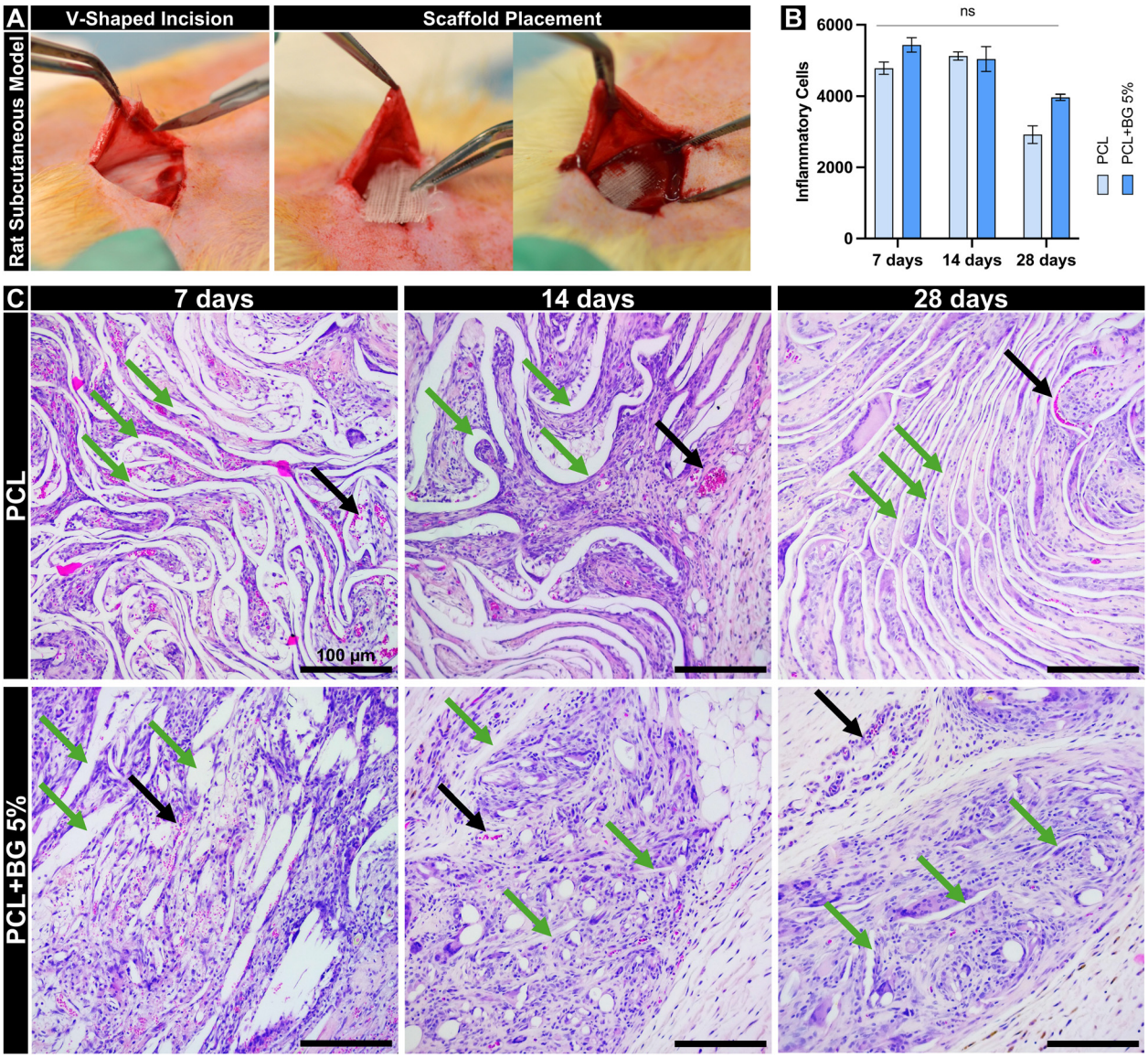

Fig. 5 (A) Pictures of the surgical procedure utilized for the subcutaneous implantation of scaffolds in rats. (B) Bar graph demonstrating the average and standard deviation of the total inflammatory cell count observed within and surrounding the scaffolds upon their retrieval. (C) Images depicting the histological features of both pure polycaprolactone (PCL) scaffolds and those enriched with 5% BG (PCL + BG5%) after retrieval. Magnification 10× – scale bar: 100 µm. Green arrows indicate the scaffolds (SC), and black arrows indicate the blood vessel formation. Notably, the pure PCL scaffolds exhibit a more structured layering pattern than those with BG. Although PCL + BG5% scaffolds displayed a higher inflammatory cell count, these differences were not statistically significant (two-way ANOVA with Šídák's multiple comparisons test, ns = not significant).

From a chemical perspective, PCL presents a hydrophobic behavior, so the scaffolds are frequently treated with sodium hydroxide (NaOH) to improve their hydrophilicity.[16,43] In the present study, a notable hydrophilicity of PCL was observed by adding BG into the polymer, confirmed by the presence of hydroxyl groups (–OH) in the FTIR spectrum, dismissing the surface treatment with NaOH after the printing process. Typical absorbance bands identifying the characteristic chemical stretches (C–C, C–O, and C═O) were found for pure PCL, confirming the expected spectrum for the polymer.[47] The increase of PCL hydrophilicity was also reported previously when incorporated with 58S-BG, confirming the results obtained in this study.[19] Raman spectroscopy revealed the bioactive structure of BG powder, enhancing its interaction with other chemical components and enabling it to bind with natural tissues, as previously mentioned.

Cytocompatibility is crucial for tissue engineering scaffolds, ensuring proper cell adhesion, spreading, and enhanced activity over time.[24,48] In this study, neither group was cytotoxic, and the presence of BG significantly improved cell viability compared to pure PCL scaffolds, likely due to BG's potent bioactivity and biological potential. Other studies also confirm 58S-BG's biocompatibility, whether in pure form or blended with polymers.[19,49] Furthermore, BG-laden scaffolds increased

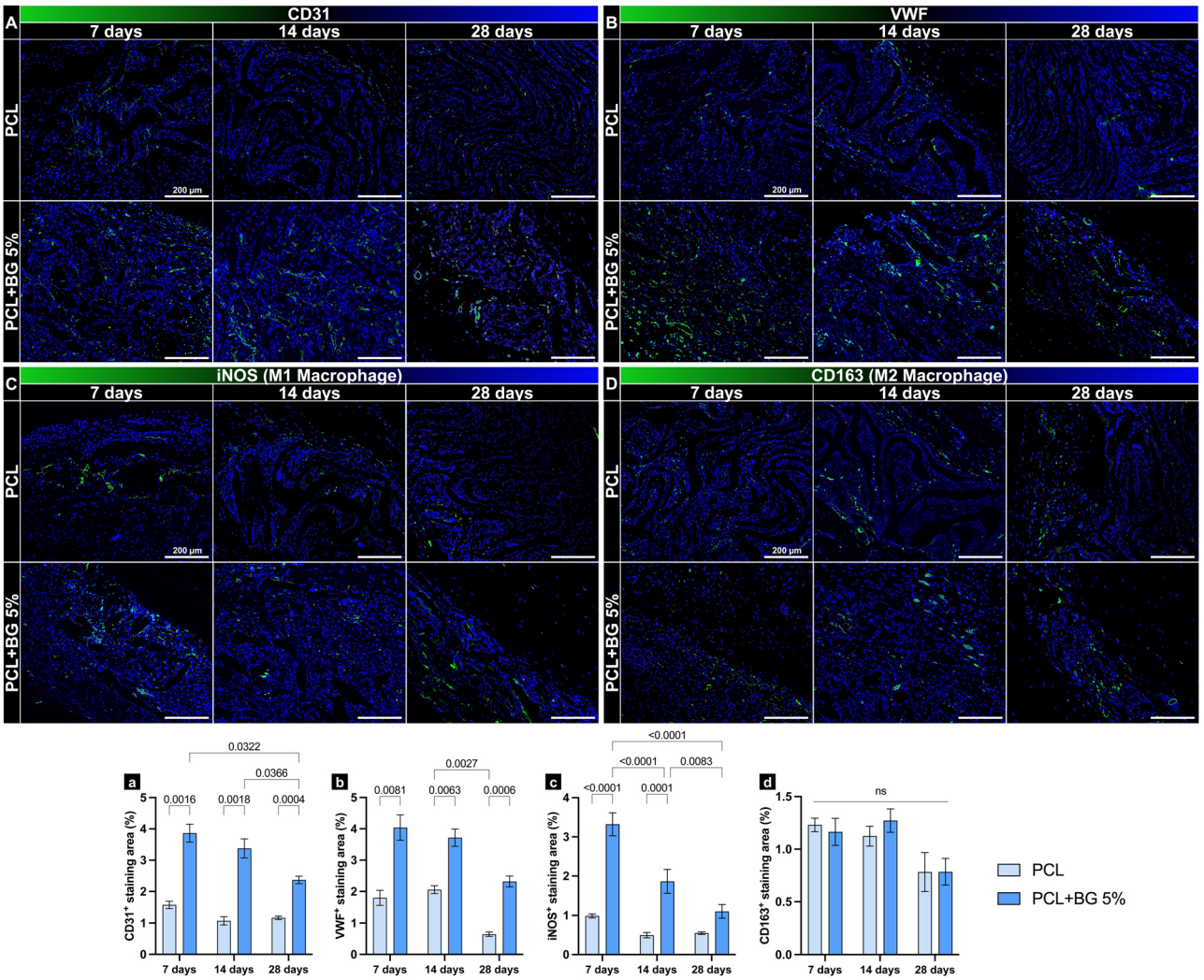

Fig. 6 *In vivo* immunolabeling of angiogenesis markers CD31 (A) and vWF (B), and macrophage polarization markers iNOS (C) and CD163 (D) was performed using Alexa Fluor 488 (green) at 7-, 14-, and 28-days post-implantation (10× magnification). PCL + BG5% implants showed significantly higher angiogenic marker (CD31 and vWF) levels and an early increase in M1 (iNOS) that diminished over time. Bar graphs (a)–(d) present mean ± SD and are analyzed using two-way ANOVA with Sidak's post-hoc test. Statistically significant differences are indicated by *p*-values; "ns" denotes non-significant differences.

aBMSC adhesion and spreading at days 1, 3, and 7, consistent with findings reported for other BG-containing scaffolds.[29,50,51] This improvement may be attributed to Ca release, increased scaffold hydrophilicity, and the rougher surface resulting from BG incorporation, which foster greater cell attachment.[41,45,52] Notably, hydrophilic surfaces can improve cell adhesion to biomaterials, supporting proliferation and differentiation,[53] which was also significantly improved on BG-laden scaffolds.

The osteogenic potential of the scaffolds was assessed by ALP activity and mineralized nodule formation assays, which are widely used *in vitro* analyses to assess osteogenic differentiation. ALP activity is an early sign of osteogenic differentiation of mesenchymal stem cells into osteoprogenitor cells, contributing significantly to the mineralization of the extracellular matrix.[41,54] Herein, it was observed that the presence of BG on the scaffolds significantly decreased the ALP activity under basal medium conditions. However, it did not impair the osteogenic differentiation under osteogenic medium conditions since ALP activity was maintained compared to pure PCL. It has been suggested that BG might not significantly impact cell differentiation but promotes new bone formation through indirect processes such as stimulating angiogenesis and bone maturation.[55] Furthermore, mineral nodule deposition (Alizarin Red) assay is used to evaluate the final results expected for bone regeneration, being considered the gold standard assay for quantifying mineralization potential *in vitro*.[56] The nodule deposition was positively influenced by the presence of BG, demonstrating that the particles significantly induce the nucleation and growth of an apatite layer even in the presence of non-osteogenic media.[41,57]

Additionally, we implanted the scaffolds in rats' subcutaneous tissue to assess their *in vivo* behavior and the resulting inflammatory response. Although the implantation site does not replicate the intended target area, this initial evaluation

provides essential data for the material's behavior before applying it in more complex, biomimetic environments. Regarding inflammation, both groups elicited comparable levels of immune reaction, characterized by the increased response in the initial days, usually due to the surgical procedure. As the healing time progressed, inflammation attenuated, and although the pure PCL group showed less inflammation, this response was not significantly different from the BG group. Previous research has demonstrated that 58S bioglass exhibits favorable local biocompatibility and no cytotoxicity to major organs. In a rat model, the bioglass was evaluated for potential effects on the gastrointestinal tract (stomach, duodenum, jejunum, and ileum) and major organs (heart, liver, spleen, lung, and kidneys). Comparisons with a control group revealed no apparent toxic signs in the gastrointestinal or major organ tissues among rats receiving bioglass. These findings indicate that the 58S bioglass does not induce *in vivo* toxicity and possesses good biocompatibility.[58]

The immunolabeling results highlight that BG incorporation enhances angiogenesis and prompts an initial, transient inflammatory response without long-term adverse effects. Specifically, endothelial markers CD31 and vWF were consistently more abundant in PCL + BG5% implants than in PCL-only scaffolds, demonstrating that BG supports neovascularization. Although early iNOS expression, an indicator of M1-mediated inflammation, was higher in PCL + BG5% scaffolds, this elevation subsided over time, pointing to a self-limiting inflammatory phase that facilitated tissue remodeling rather than hindering it. Meanwhile, the comparable CD163 levels in both groups indicate that BG does not disrupt the eventual transition toward M2-driven inflammation resolution. M1 macrophages are activated by pro-inflammatory signals, such as interferon (IFN-γ) and tumor necrosis factor (TNF-α), released following tissue damage evoked by scaffold implantation. This early activation supports phagocytosis and initiates angiogenesis; however, prolonged M1 activity leads to chronic inflammation, severe foreign body responses, and fibrous encapsulation, ultimately impeding tissue healing. Recent studies emphasize that M1 macrophages contribute to stem cell recruitment, early angiogenesis, and osteointegration, but timely polarization away from the M1 state is essential.[59] Our findings suggest that the enhanced angiogenesis observed in the BG group is likely due to a transient rise in M1 macrophage levels sufficient to improve vascularization without compromising biocompatibility. This response, together with earlier research demonstrating the bone-forming capabilities of 58S BG, such as its ability to promote osseous filling in critical-sized cancellous defects without eliciting adverse tissue reactions in a rabbit model, supports the safe progression of testing these scaffolds in additional *in vivo* models.[37,60]

Finally, it is essential to highlight the advantages of MEW in producing scaffolds for tissue regeneration, gathering the most significant benefits of 3D printing, such as manufacturing precise and personalized scaffolds with also a micro- and nano-scale structure, with thin and highly aligned filaments, which will be appropriately penetrated by the desired cells to induce bone formation. Thus, with the ability to incorporate BG particles to improve bioactivity, the composition presented in this study is an excellent alternative for enhancing bone regeneration. Further investigations are encouraged to cover this study's limitations, such as additional *in vitro* assays that could provide molecular insights about the biological behavior of BG-laden scaffolds. Besides that, the bioengineering field is constantly expanding, and there is still a lot to be investigated, such as developing graded scaffolds or the printability of other polymers containing BG to broaden the applications of MEW for bone tissue engineering.

5. Conclusion

PCL scaffolds incorporated with 58S-BG particles were successfully fabricated by the melt electrowriting technique, retaining the architecture and appropriate fiber alignment. These scaffolds exhibit favorable properties, such as enhanced cell viability and adhesion, overcoming the hydrophobic limitation of pure PCL scaffolds. They also demonstrated desirable properties *in vitro* and *in vivo*, showing approximately a two-fold increase in mineral nodule deposition after 21 days and a two-fold immunolabeling of angiogenic markers, positioning them as promising scaffolds for bone regeneration.

Author contributions

Ana Beatriz G. de Carvalho: investigation, formal analysis, data curation, writing – original draft, funding acquisition; Lais M. Cardoso: formal analysis, data curation, investigation, methodology; Caroline Anselmi: formal analysis, data curation, investigation, methodology; Renan Dal-Fabbro: data curation, investigation, methodology, writing – reviewing and editing; Tiago M. B. Campos: methodology, writing – reviewing and editing; Alexandre L. S. Borges: conceptualization, validation, writing – reviewing and editing; Guilherme S. F. A. Saavedra: conceptualization, validation, writing – reviewing and editing; and Marco C. Bottino: conceptualization, project administration, validation, funding acquisition, writing – reviewing and editing, supervision, project administration.

Data availability

All data generated or analyzed during this study are included in this published article.

Conflicts of interest

The authors declare that they have no competing interests.

Acknowledgements

This study was funded by the Sao Paulo State Research Foundation (FAPESP) (grant # 2022/03811-9) and the National Institutes of Health (NIH – National Institute of Dental and

Craniofacial Research/NIDCR, grant R01DE031476). The authors acknowledge the University of Michigan College of Engineering and the Michigan Center for Materials Characterization for SEM images. The authors also acknowledge Biorender for the schematic images used in the graphical abstract.

References

1 Z. Aytac, N. Dubey, A. Daghrery, J. A. Ferreira, I. J. de Souza Araujo, M. Castilho, J. Malda and M. C. Bottino, *Int. Mater. Rev.*, 2022, **67**, 347–384.
2 E. Babaie and S. B. Bhaduri, *ACS Biomater. Sci. Eng.*, 2018, **4**, 1–39.
3 M. Anderson, N. Dubey, K. Bogie, C. Cao, J. Li, J. Lerchbacker, G. Mendonça, F. Kauffmann, M. C. Bottino and D. Kaigler, *Dent. Mater.*, 2022, **38**, 529–539.
4 L. Cheng, K. S. Suresh, H. He, R. S. Rajput, Q. Feng, S. Ramesh, Y. Wang, S. Krishnan, S. Ostrovidov, G. Camci-Unal and M. Ramalingam, *Int. J. Nanomed.*, 2021, **16**, 4289–4319.
5 O. Tao, J. Kort-Mascort, Y. Lin, H. M. Pham, A. M. Charbonneau, O. A. ElKashty, J. M. Kinsella and S. D. Tran, *Micromachines*, 2019, **10**(7), 480.
6 T. D. Brown, P. D. Dalton and D. W. Hutmacher, *Adv. Mater.*, 2011, **23**, 5651–5657.
7 A. Daghrery, I. J. de Souza Araujo, M. Castilho, J. Malda and M. C. Bottino, *Acta Biomater.*, 2023, **156**, 88–109.
8 A. Daghrery, J. A. Ferreira, J. Xu, N. Golafshan, D. Kaigler, S. B. Bhaduri, J. Malda, M. Castilho and M. C. Bottino, *Bioact. Mater.*, 2023, **19**, 268–281.
9 K. F. Eichholz, F. E. Freeman, P. Pitacco, J. Nulty, D. Ahern, R. Burdis, D. C. Browe, O. Garcia, D. A. Hoey and D. J. Kelly, *Biofabrication*, 2022, **14**, 045013.
10 J. C. Kade and P. D. Dalton, *Adv. Healthcare Mater.*, 2021, **10**, 2001232.
11 A. Hrynevich, B. Elçi, J. N. Haigh, R. McMaster, A. Youssef, C. Blum, T. Blunk, G. Hochleitner, J. Groll and P. D. Dalton, *Small*, 2018, **14**, e1800232.
12 N. Dubey, J. A. Ferreira, A. Daghrery, Z. Aytac, J. Malda, S. B. Bhaduri and M. C. Bottino, *Acta Biomater.*, 2020, **113**, 164–176.
13 Z. Chen, Y. Liu, J. Huang, M. Hao, X. Hu, X. Qian, J. Fan, H. Yang and B. Yang, *N. Engl. J. Med.*, 2022, **14**(6), 3404.
14 M. Castilho, A. van Mil, M. Maher, C. H. G. Metz, G. Hochleitner, J. Groll, P. A. Doevendans, K. Ito, J. P. G. Sluijter and J. Malda, *Adv. Funct. Mater.*, 2018, **28**, 1803151.
15 N. Siddiqui, S. Asawa, B. Birru, R. Baadhe and S. Rao, *Mol. Biotechnol.*, 2018, **60**, 506–532.
16 M. A. Woodruff and D. W. Hutmacher, *Prog. Polym. Sci.*, 2010, **35**, 1217–1256.
17 C. Blum, K. Schlegelmilch, T. Schilling, A. Shridhar, M. Rudert, F. Jakob, P. D. Dalton, T. Blunk, L. E. Flynn and J. Groll, *ACS Biomater. Sci. Eng.*, 2019, **5**, 6655–6666.
18 N. Golafshan, M. Castilho, A. Daghrery, M. Alehosseini, T. van de Kemp, K. Krikonis, M. de Ruijter, R. Dal-Fabbro, A. Dolatshahi-Pirouz, S. B. Bhaduri, M. C. Bottino and J. Malda, *ACS Appl. Mater. Interfaces*, 2023, **15**, 12735–12749.
19 C. C. L. Guimarães, J. R. de Souza, T. M. B. Campos, T. O. Marques, L. T. Kito, E. C. Kukulka, L. M. R. de Vasconcellos, A. L. S. Borges and G. P. Thim, *J. Biomed. Mater. Res., Part B*, 2024, **112**, e35315.
20 A. Abdal-hay, N. A. Kocak-Oztug, F. A. Sheikh, P. Han, S. Anwar, B. P. J. Fournier and S. Ivanovski, *Colloids Surf., B*, 2025, **245**, 114270.
21 F. Baino, G. Novajra and C. Vitale-Brovarone, *Front. Bioeng. Biotechnol.*, 2015, **3**, 202.
22 X. Zhang, Y. Li, Z. Ma, D. He and H. Li, *Bioact. Mater.*, 2021, **6**, 3692–3704.
23 G. Hochleitner, M. Kessler, M. Schmitz, A. R. Boccaccini, J. Teßmar and J. Groll, *Mater. Lett.*, 2017, **205**, 257–260.
24 Y. Cai, X. Sun, Q. Feng, B. Li, X. Li, S. Chen, X. Zhou and C. He, *Composites, Part B*, 2024, **286**, 111771.
25 F. Baino and C. Vitale-Brovarone, *J. Biomed. Mater. Res., Part A*, 2011, **97**, 514–535.
26 V. C. P. F. Aguiar, R. d N. Bezerra, K. W. dos Santos, I. d S. Gonçalves, K. J. S. G. Costa, D. P. Lauda, T. M. B. Campos, R. F. do Prado, L. M. R. de Vasconcellos and I. R. de Oliveira, *J. Biomater. Sci., Polym. Ed.*, 2024, **35**, 1493–1510.
27 E. Motalebzadeh, S. Hemati, M. A. Mayvani and M. Ghollasi, *Mol. Biol. Rep.*, 2024, **51**, 838.
28 E. C. Kukulka, J. R. de Souza, J. C. R. de Araújo, L. M. R. de Vasconcellos, T. M. B. Campos, G. P. Thim and A. L. S. Borges, *J. Biomed. Mater. Res., Part B*, 2023, **111**, 140–150.
29 J. R. de Souza, E. C. Kukulka, J. C. R. Araujo, T. M. B. Campos, R. F. do Prado, L. M. R. de Vasconcellos, G. P. Thin and A. L. S. Borges, *J. Biomed. Mater. Res., Part B*, 2023, **111**, 151–160.
30 A. H. Mahmoud, Y. Han, R. Dal-Fabbro, A. Daghrery, J. Xu, D. Kaigler, S. B. Bhaduri, J. Malda and M. C. Bottino, *ACS Appl. Mater. Interfaces*, 2023, **15**, 32121–32135.
31 S. Mason, S. A. Tarle, W. Osibin, Y. Kinfu and D. Kaigler, *J. Dent. Res.*, 2014, **93**, 55–61.
32 P. T. A. Toledo, C. Anselmi, R. Dal-Fabbro, A. H. Mahmoud, A. K. Abel, M. L. Becker, A. C. B. Delbem and M. C. Bottino, *J. Funct. Biomater.*, 2023, **14**, 350.
33 J. S. Ribeiro, E. A. F. Bordini, J. A. Ferreira, L. Mei, N. Dubey, J. C. Fenno, E. Piva, R. G. Lund, A. Schwendeman and M. C. Bottino, *ACS Appl. Mater. Interfaces*, 2020, **12**, 16006–16017.
34 A. A. Ayoub, A. H. Mahmoud, J. S. Ribeiro, A. Daghrery, J. Xu, J. C. Fenno, A. Schwendeman, H. Sasaki, R. Dal-Fabbro and M. C. Bottino, *Int. J. Mol. Sci.*, 2022, **23**, 13761.
35 S. S. Namazi, A. H. Mahmoud, R. Dal-Fabbro, Y. Han, J. Xu, H. Sasaki, J. C. Fenno and M. C. Bottino, *Biomater. Adv.*, 2023, **150**, 213427.
36 R. Dal-Fabbro, M. Yu, L. Mei, H. Sasaki, A. Schwendeman and M. C. Bottino, *Int. J. Oral Sci.*, 2024, **16**, 50.
37 H. Li, S. Chen, Y. Wu, J. Jiang, Y. Ge, K. Gao, P. Zhang and L. Wu, *Int. Orthop.*, 2012, **36**, 191–197.
38 W. Cao and L. L. Hench, *Ceram. Int.*, 1996, **22**, 493–507.

39 R. C. Bielby, I. S. Christodoulou, R. S. Pryce, W. J. P. Radford, L. L. Hench and J. M. Polak, *Tissue Eng.*, 2004, **10**, 1018–1026.
40 C. Mao, X. Chen, G. Miao and C. Lin, *Biomed. Mater.*, 2015, **10**, 025005.
41 B. N. Singh and K. Pramanik, *Biofabrication*, 2017, **9**, 015028.
42 X. Chen, N. Karpukhina, D. S. Brauer and R. G. Hill, *Biomed. Glasses*, 2015, **1**, 108–118.
43 A. Daghrery, J. A. Ferreira, I. J. de Souza Araujo, B. H. Clarkson, G. J. Eckert, S. B. Bhaduri, J. Malda and M. C. Bottino, *Adv. Healthcare Mater.*, 2021, **10**, e2101152.
44 N. Abbasi, S. Ivanovski, K. Gulati, R. M. Love and S. Hamlet, *Biomater. Res.*, 2020, **24**, 2.
45 H.-Y. Shen, F. Xing, S.-Y. Shang, K. Jiang, M. Kuzmanović, F.-W. Huang, Y. Liu, E. Luo, M. Edeleva, L. Cardon, S. Huang, Z. Xiang, J.-Z. Xu and Z.-M. Li, *ACS Appl. Mater. Interfaces*, 2024, **16**, 18658–18670.
46 J. Wang, Q. Yang, Q. Saiding, L. Chen, M. Liu, Z. Wang, L. Xiang, L. Deng, Y. Chen and W. Cui, *Adv. Sci.*, 2023, **10**, 2304111.
47 T. Zehnder, T. Freund, M. Demir, R. Detsch and A. R. Boccaccini, *Materials*, 2016, **9**(11), 887.
48 M. J. Gupte and P. X. Ma, *J. Dent. Res.*, 2012, **91**, 227–234.
49 E. Saino, S. Grandi, E. Quartarone, V. Maliardi, D. Galli, N. Bloise, L. Fassina, M. G. De Angelis, P. Mustarelli, M. Imbriani and L. Visai, *Eur. Cells Mater.*, 2011, **21**, 59–72; discussion 72.
50 V. V. Meretoja, A. O. Helminen, J. J. Korventausta, V. Haapaaho, J. V. Seppälä and T. O. Närhi, *J. Biomed. Mater. Res., Part A*, 2006, **77A**, 261–268.
51 A. Shahin-Shamsabadi, A. Hashemi, M. Tahriri, F. Bastami, M. Salehi and F. Mashhadi Abbas, *Mater. Sci. Eng., C: Mater. Biol. Appl.*, 2018, **90**, 280–288.
52 N. Saranya, S. Saravanan, A. Moorthi, B. Ramyakrishna and N. Selvamurugan, *J. Biomed. Nanotechnol.*, 2011, **7**, 238–244.
53 R. Teimouri, K. Abnous, S. M. Taghdisi, M. Ramezani and M. Alibolandi, *J. Mater. Res. Technol.*, 2023, **24**, 7938–7973.
54 S. Vimalraj, *Gene*, 2020, **754**, 144855.
55 J. Kent Leach, D. Kaigler, Z. Wang, P. H. Krebsbach and D. J. Mooney, *Biomaterials*, 2006, **27**, 3249–3255.
56 A. Bernar, J. V. Gebetsberger, M. Bauer, W. Streif and M. Schirmer, *Int. J. Mol. Sci.*, 2023, **24**(1), 723.
57 G. F. da Fonseca, S. d O. M. Avelino, D. d C. R. Mello, R. F. do Prado, T. M. B. Campos, L. M. R. de Vasconcellos, E. de Sousa Trichês and A. L. S. Borges, *J. Mater. Sci.: Mater. Med.*, 2020, **31**, 41.
58 W. Wang, S. Jia, G. Miao, Z. Sun, F. Yu, Z. Gao and Y. Li, *Biomater. Adv.*, 2023, **152**, 213520.
59 K. Zheng, W. Niu, B. Lei and A. R. Boccaccini, *Acta Biomater.*, 2021, **133**, 168–186.
60 D. L. Wheeler, E. J. Eschbach, R. G. Hoellrich, M. J. Montfort and D. L. Chamberland, *J. Orthop. Res.*, 2000, **18**, 140–148.